

# *Correlation of Neutron-Based Strain Imaging and Mechanical Behavior of Armor Steel Welds Produced with the Hybrid Laser Arc Welding Process*

Jeffrey W. Sowards<sup>1</sup>, Daniel S. Hussey<sup>2</sup>, David L. Jacobson<sup>2</sup>, Stan Ream<sup>3</sup>, and Paul Williams<sup>4</sup>

<sup>1</sup>NASA, Marshall Space Flight Center,  
Huntsville, AL 35812, USA

<sup>2</sup>National Institute of Standards and Technology,  
Gaithersburg, MD 20899, USA

<sup>3</sup>EWI,  
Columbus, OH 43221, USA

<sup>4</sup>National Institute of Standards and Technology,  
Boulder, CO 80305, USA

[jeffrey.w.sowards@nasa.gov](mailto:jeffrey.w.sowards@nasa.gov)  
[daniel.hussey@nist.gov](mailto:daniel.hussey@nist.gov)  
[david.jacobson@nist.gov](mailto:david.jacobson@nist.gov)  
[sream@ewi.org](mailto:sream@ewi.org)  
[paul.williams@nist.gov](mailto:paul.williams@nist.gov)

Bragg edge neutron transmission imaging was used to characterize the spatial distribution of thermally induced residual strains in a steel armor plate welded with a hybrid laser arc process. This residual strain distribution was compared to the spatial development of mechanical strain during uniaxial deformation. By correlating the strain measurements of both methods, the failure mechanism was determined in armor welds joined with this process. Weld failure consistently occurred in the subcritical heat-affected zone where mechanical strain accumulation in softened martensitic parent material was superimposed upon the weld region containing the highest residual thermally induced strain.

**Key words:** armor steel; Bragg edge; digital image correlation; hybrid laser welding; neutron diffraction; residual strain.

**Accepted:** May 18, 2018

**Published:** June 11, 2018

<https://doi.org/10.6028/jres.123.011>

---

## 1. Introduction and Background

The hybrid laser arc welding process (HLAW) combines a laser heat source and a gas metal arc welding heat source to overcome many of the limitations encountered when using either welding process by itself. These advantages include increased welding speed, the ability to weld thicker materials, the ability to better bridge gaps when part fit-up is poor, better weld quality, and greater stability of the welding

process [1]. The deep penetration ability of the laser heat source may also be beneficial in reducing the need for multiple-pass welding. The process is gaining wider recognition as a viable welding process as more materials are successfully welded. Several studies [2–8] evaluating the application of various welding processes to joining high-strength armor steels have shown the importance of minimizing the width of the welding heat-affected zone, which correlates with improved ballistic resistance as tempering of martensitic base metal occurs, leading to softening. The benefits of the steeper thermal gradient of HLAW (compared to arc welding alone) and gap bridging ability make the process of great interest [7].

However, thermal residual stresses in HLAW do develop as a result of the nonuniform heating and cooling during welding [9], and welding residual stress can lead to performance degradation by various mechanisms. Welds of steel armor plate (MIL-A-46100) have exhibited cracking after field service, with the cause ultimately attributed to stress-corrosion cracking, hydrogen-assisted cold cracking, and harsh vehicle usage [10]. Therefore, a better understanding of welding-induced thermal stresses can mitigate damage by precluding those forms of cracking. Several modeling efforts have been directed to the process to evaluate heat transfer and subsequent microstructural and residual stress evolution [6, 9]. X-ray diffraction was used in the latter study to experimentally determine residual stresses in steel hybrid laser arc (HLA) welds for validation of numerical simulations [9]. However, only qualitative comparisons were made in that study, since X-rays only probe the surface [9]. Low residual stresses and distortion, and subsequent cracking resistance, have been realized with the HLAW process, since low heat input per unit length is achieved by the laser heating source [11]. In addition to residual stress control, microstructures in steel can be controlled by adjusting cooling rate and weld metal composition, giving hybrid processes an advantage over laser welding alone. Weld cooling rates (to cool from 800 °C to 500 °C) in hybrid welding of steel are close to, albeit slower than, those of laser welding alone [12]. The additional heat input from multiple heat sources during hybrid process welding reduces the cooling rate, thereby reducing hardening of higher-strength steel [11].

Here, we apply a novel technique for characterizing weld strain in two dimensions that measures lattice strain in the crystallographic structure using neutron diffraction. The Bragg edge method has been presented as an instrumental technique to study strain distribution in fusion welds [13, 14]; however, past studies did not correlate spatially varying strain data to mechanical behavior. The structure-property relationship of HLA welded armor steel is demonstrated here, where the Bragg edge is used to characterize thermally induced strains resulting from the welding process, which are then correlated to the spatial distribution of hardness and mechanical strain behavior during loading in uniaxial tension.

## 2. Experiments

The 9.8 mm thick plate of MIL-A-46100 was welded at EWI (Columbus, OH) using the HLAW process. Base metal was received in quenched and tempered condition with hardness of  $\sim 542$  HV<sub>1.0</sub>. Gas metal arc welding current and voltage were held constant at 260 amps and 26 volts, respectively, while ER-60 filler metal was deposited into the joint. Fiber laser power was set to 10 kW, and the welding process was traversed along the butt weld at 33.9 mm s<sup>-1</sup> travel speed. A shielding gas mixture of 90 % Ar–10 % CO<sub>2</sub> was directed across the weld at a flow rate of 23.6 L min<sup>-1</sup>. A schematic of the weld plate geometry is shown in Fig. 1a. Test specimens were sectioned from the plate at indicated locations using wire electron discharge machining. Metallographic specimens were prepared with standard techniques and etched with 2 vol. % nitric acid solution (Nital). Chemistry (wt. %) of the base material was measured by a certified analytical laboratory (0.29C-0.74Mn-0.46Ni-0.51Cr-0.21Mo-0.006V-0.0015B-0.032Cu-0.004N-0.032Ti-0.001Zr-0.027Al). Weld fusion zone (FZ) chemistry was measured also, but due to high dilution by the base metal, the FZ composition was nearly identical to base metal. The difference in carbon weight percent was 0.29 wt% in the base vs 0.30 wt% in the weld, resulting in a maximum shift in the lattice spacing equivalent to 400 με. Two-dimensional hardness maps were determined by calibrated Vickers indentation (1 kg force) at a spacing of 200 μm.

Weld strap specimens (3.8 mm thick) were machined and coated with a flat white base layer followed by application of a black speckle pattern. Specimens were tested in tension until failure using a closed-loop servohydraulic universal test frame (250 kN maximum force capacity) at a constant actuator displacement rate of 0.3 mm min<sup>-1</sup>. A stereo digital camera system was used to record the speckle patterns at a frame capture rate of 1 s<sup>-1</sup>. The digital images were processed with commercially available digital image correlation (DIC) software to determine the surface strain distribution. The uncertainty in the strain from the image correlations was about 280  $\mu\epsilon$ .

Specimens with dimensions of 20 mm  $\times$  60 mm  $\times$  9.8 mm were removed from the weld to study the strain distribution with neutron imaging at the National Institute of Standards and Technology (NIST) Center for Neutron Research (NCNR). Strain imaging of the samples was performed using the Bragg edge neutron transmission method [13, 15] along the  $\langle 220 \rangle$  lattice. The Bragg edge method measures strains that are parallel to the beam direction; therefore, while the tensile test reports the axial strain, the Bragg edge reports the lateral strain. Bragg edges at four tempering conditions, as received, 300 °C, 450 °C, and 690 °C, and a few beam-sample orientations were acquired. Tempering was performed in a vacuum tube furnace (MTI GSL-1100 Tube Furnace), with a ramp to temperature in 1 h, and a 1 h hold at temperature. The sample was allowed to cool to below 80 °C in vacuum. Bragg edges were acquired with a double monochromator assembly composed of two highly oriented pyrolytic graphite (HOPG) crystals, with dimensions 5 cm  $\times$  5 cm  $\times$  0.5 mm, crystal mosaic spread of 0.5°, and the (004) reflection selected in a narrow range ( $\Delta\lambda/\lambda \sim 0.01$ ) of neutron wavelengths. The neutron images were acquired using a 250  $\mu\text{m}$  thick ZnS:LiF scintillator screen, viewed by an Andor Neo sCMOS (scientific complementary metal-oxide semiconductor) camera with an effective pixel pitch of 75  $\mu\text{m}$ . At each wavelength, five images were acquired, each with an exposure time of 100 s. Images were acquired over the wavelength range 0.19950 nm to 0.20575 nm with a step size of 0.00025 nm. An error function (ERF) of the form

$$\text{constant} + \text{amplitude} \times \text{ERF}[(\lambda - \lambda_B)/(\sqrt{2} \times \sigma)]$$

was fit to the intensity variation as a function of wavelength using a nonlinear least square algorithm with a reduced chi-squared quality of fit between 0.9 and 1.1 (1.0 average across the sample). The average relative uncertainty (one standard deviation from the fit) in the Bragg edge ( $\lambda_B$ ) was  $5 \times 10^{-4}$  nm, providing a strain resolution of about 250  $\mu\epsilon$ . Unstrained base metal (location shown in Fig. 1a but results not given in Fig. 2) was used to determine the unstrained lattice spacing; in the as-received state, the average unstrained lattice spacing was 0.202274(2) nm, where the uncertainty is the one-sigma root mean square error from a region of interest comprising 3300 pixels.

### 3. Results and Discussion

Metallographic cross sections (Fig. 1b) revealed a narrow FZ near the midthickness location of the plate and more pronounced cap and root. The microstructure of the FZ was predominantly martensitic and contained some ferrite and bainite that varied spatially throughout the weld. This spatial variation of microstructure was likely caused by variations in cooling rate driven by the unique shape of the weld, which in turn was induced by the fluid-flow behavior unique to HLAW [11]. Results of hardness mapping (Fig. 1c) were more revealing; they better distinguished the spatial variation of the microstructure throughout the weldment. In general, FZ hardness was only slightly less than that of the base metal, particularly at the cap and near the centerline. Arc welding has also resulted in undermatching hardness in the weld compared to base metal [2, 3], though the extent reported here is lower. The weld cap had the lowest hardness (350 to 400 HV), whereas the root had the highest hardness (500 HV) in the FZ. Faster cooling rate is likely in the root (numerical modeling has predicted that the thermal gradient is steeper at

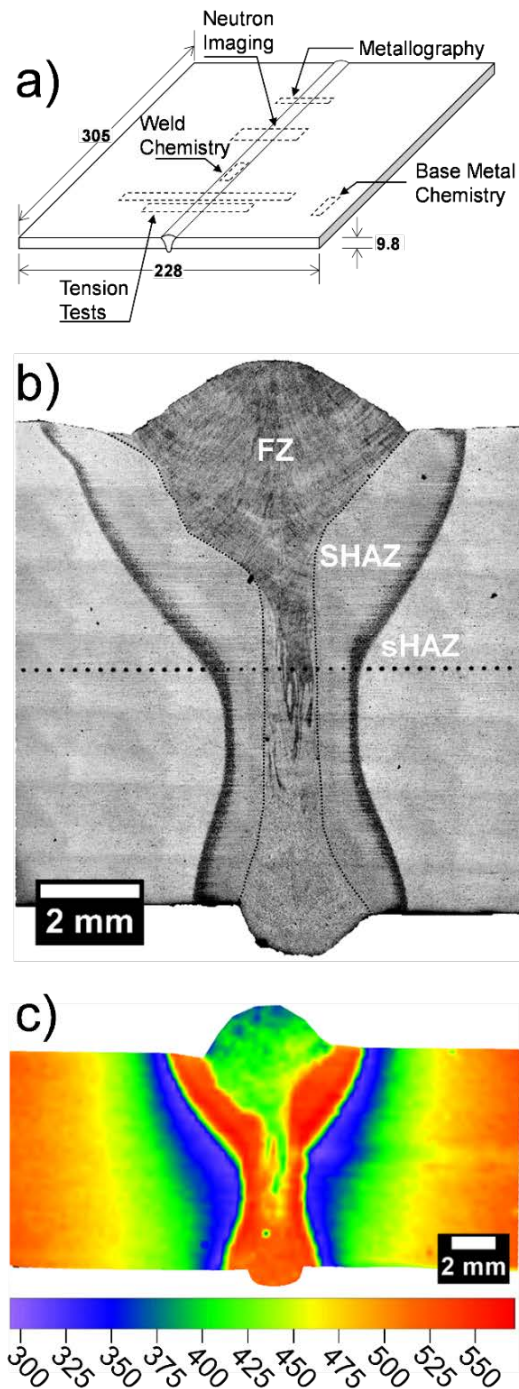


**Fig. 1.** (a) Armor plate weld geometry and sampling locations for structure-property characterization (dimensions in mm). (b) Metallographic mosaic showing cross section of hybrid laser arc weld on armor plate. Fusion zone (FZ), supercritical heat-affected zone (SHAZ), and subcritical heat-affected zone (sHAZ) are indicated. (c) Vickers microhardness ( $\text{kgf}/\text{mm}^2$ ) map of weld cross section.

the root near the fusion boundary relative to the cap [9]), resulting in the greatest fraction of martensite in that particular location within the FZ. Outside of the FZ in the supercritical heat-affected zone (HAZ; i.e., where the peak temperature of the weld is less than the intercritical temperature,  $T_{\text{peak}} > A_1$ ), there was a pronounced hardening (up to 550 HV) due to formation of fresh, high-hardness martensite formed upon weld cooling. The width of the supercritical HAZ region was less than about 2 mm when measured from the fusion boundary. Outside of the HAZ, a tempered martensitic structure was evident based on observed softening. In the subcritical HAZ ( $T_{\text{peak}} < A_1$ ), an abrupt drop in hardness was observed over a distance of less than 1 mm from the isotherm representing the  $A_1$  boundary. Within that steep gradient, hardness dropped from 500 HV to 300 HV, and it gradually increased again with increasing distance from the  $A_1$  isothermal boundary. This tempering effect of base metal resulted in a softened region beginning at about 2 mm from the fusion boundary. The softened region (~4 mm wide) was constrained by two harder zones (base metal and supercritical HAZ), and it was much narrower than that previously reported for gas metal arc welding (up to ~14 mm in width [2]).

Neutron transmission strain maps revealed thermally induced tensile strain adjacent to both sides of the weld FZ. A compressive strain was observed in the FZ itself, the supercritical HAZ, and the base metal outside the region containing tensile strain. Kong *et al.* predicted and observed a similar longitudinal stress state when the center of a steel weldment was placed under residual tensile stress following HLAW [9]. During Bragg edge measurements, the neutron path scatters through the entire specimen thickness (10 mm in the plane view and 20 mm in the cross section), reporting an average lattice strain along that path. Maximum through-thickness residual strains measured here (~3000  $\mu\epsilon$  max) are well below those required to induce plastic flow in the parent material, which has a yield strength of 1400 MPa. (A simple elastic deformation analysis reveals that the residual strains found here are much lower than the yield strength of the base metal:  $\sigma = E \cdot \epsilon = 204 \text{ GPa} \times 3000 \mu\epsilon = 612 \text{ MPa}$ , where  $\sigma$  denotes stress,  $E$  is elastic modulus of martensite [16], and  $\epsilon$  is strain.) The magnitude of tensile strain is quite low (500  $\mu\epsilon$  strains result in stresses of ~100 MPa). However, the specimen was cut from the parent plate prior to neutron imaging, which is expected to reduce residual strains to some extent. The  $1/e$  depth for thermal neutron penetration in iron is about 1 cm, so that the maximum specimen thickness to be analyzed with this technique is about 3 cm to 4 cm. The strain after tempering (Fig. 2c–d) shows that all the residual strain was substantially reduced after tempering at 450 °C, and it was completely relieved after the 690 °C temper. The region of martensite tempering (Fig. 1c) was much wider than the region of strain indicated by neutron imaging, suggesting that any effect of tempering on crystallographic structure is minimal.

Mechanical strain distribution measured with DIC at peak applied force (prior to necking) is shown in Fig. 3a. Locations of microstructural boundaries are evident on the maps due to nonuniform straining in those regions. Metallurgical boundaries are highlighted based on the weld cross section shown in Fig. 1b. The highest strain localization was observed in the subcritical region of the HAZ ( $T_{\text{peak}} < A_1$ ), which coincided with the greatest extent of softening induced by the welding process. The constitutive behavior of each of the regions is shown in Fig. 3b. Dashed lines along each curve represent the 0.2 % offset yield condition. Yielding was associated only with weld-induced softening, since base material outside of the subcritical HAZ did not exhibit yielding. The FZ and supercritical HAZ exhibited similar yield strength levels (~1000 MPa). The subcritical HAZ exhibited a gradient in yield strength, correlating to the gradient in hardness, where increasing strength was observed when moving away from the softest region at sHAZ1, which correlated with a thin band of ~300 HV material shown in Fig. 1c. The yield strength of the soft zone was as low as 980 MPa and increased to 1120 MPa closer to the base metal. Specimens were strained until fracture, revealing ductile initiation at the weld root in softened subcritical HAZ. Shortly after ductile initiation adjacent to the weld root, rapid brittle fracture followed along the band of softest martensite. This mixed fracture mode occurred identically in all six tensile tests performed.

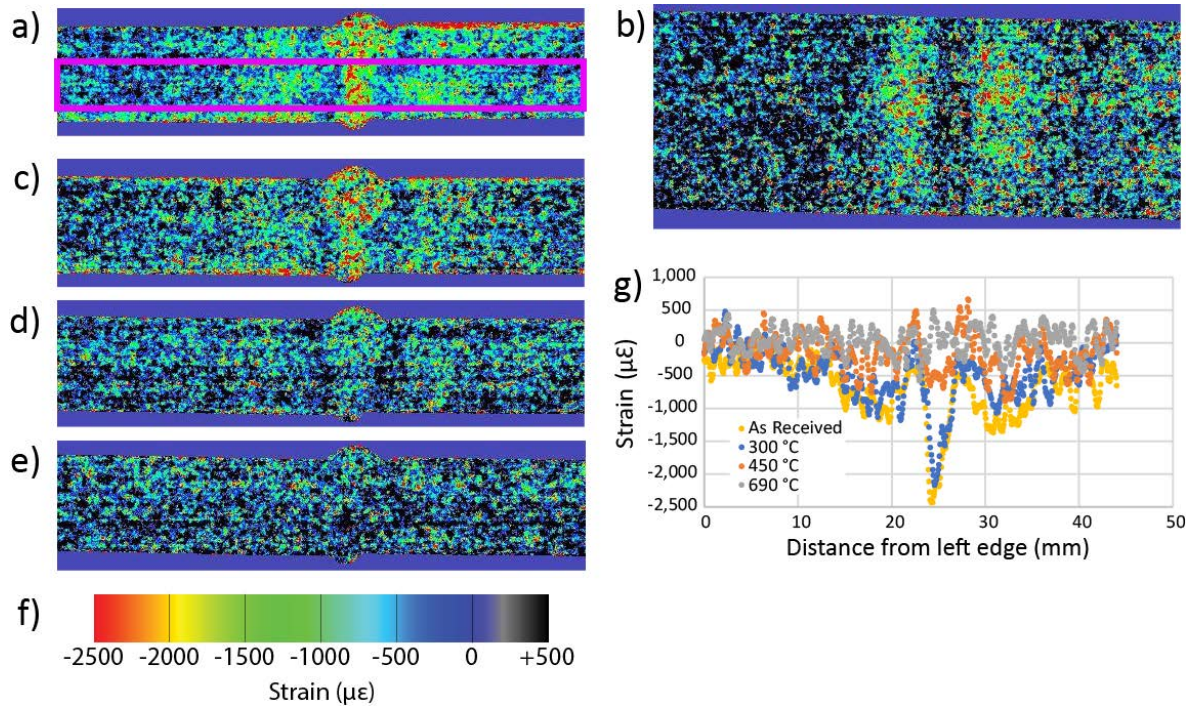


**Fig. 2.** Strain maps determined from neutron Bragg-edge measurement of the weld in the (a) cross-section and (b) plan-view orientation for the as-received sample. The effect of tempering on the strain is shown for the cross-section view after tempering at 300 °C (c), (d) 450 °C, and (e) 690 °C. The color scale for the strain is in (f). The strain maps show tensile residual strain in the heat-affected zone and compressive strain in the weld fusion zone and the release of the stress upon tempering, and this shown in the line plot (g), which is the average strain from left to right shown over the region of interest indicated by the box in (a).

Interestingly, it has been proposed that ballistic performance is improved when the softened region of the subcritical HAZ is narrow, since it is better constrained by harder surrounding structure [2]. While ballistic straining was not investigated in the current study, the behavior is shown to be more complex than a hardness change. By using the Bragg edge measurements, this study demonstrated that this region is placed under residual tensile strain, and it is surrounded by regions placed under compressive strain. Furthermore, DIC measurements demonstrated that the region is most susceptible to strain accumulation due to the softened (lower yield strength) structure and the residual tensile state. Therefore, we propose that this is not simply an effect of hardness change, but it involves the state of residual strain and straining behavior during mechanical loading.

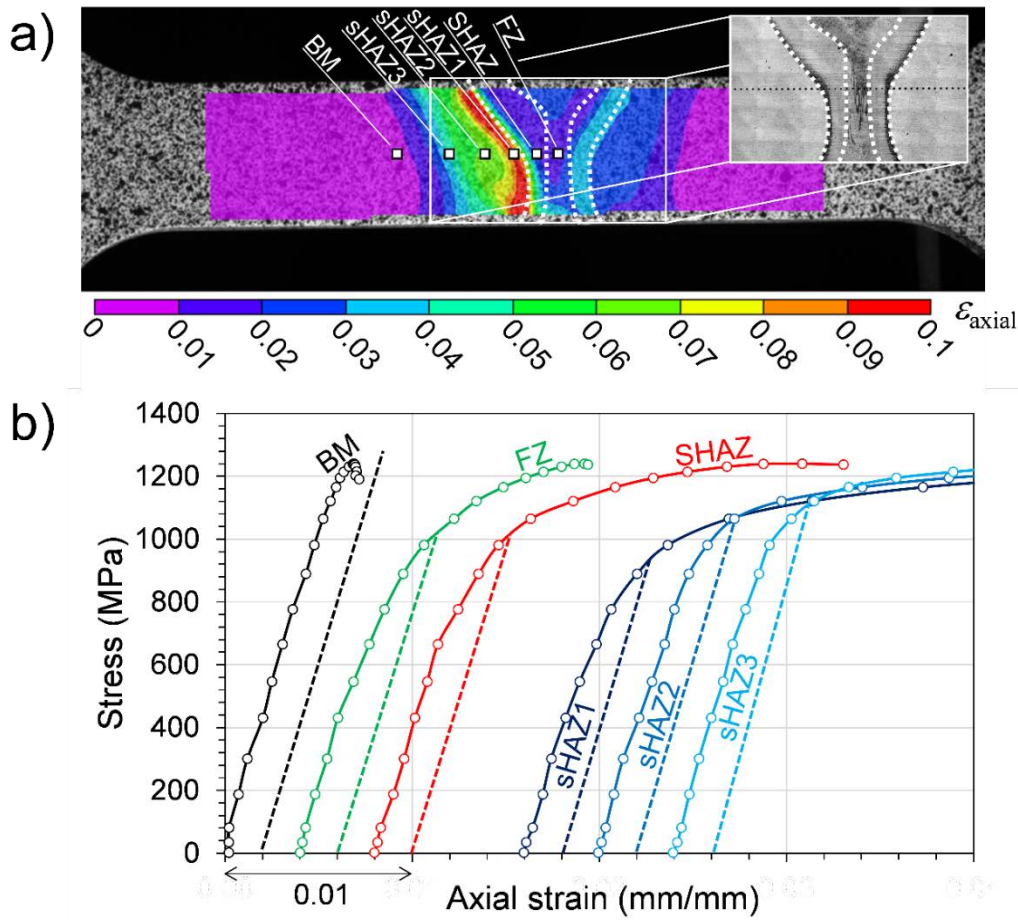


**Fig. 3.** Strain behavior determined with digital image correlation. (a) Axial strain ( $\epsilon_{\text{axial}}$  mm/mm) image of weld tensile bar at maximum force-bearing capacity (29.9 kN). (b) Constitutive response at indicated points within the various weld regions. Base metal (BM), fusion zone (FZ), supercritical heat-affected zone (SHAZ), and subcritical heat-affected zones (sHAZ) are indicated.

#### 4. Summary

Until now, the residual thermally induced strain has not been measured in armor weld materials produced with HLAW, and furthermore, it has not been correlated to mechanical behavior. This work has shown the extent of softening outside the supercritical HAZ, and imposition of thermally induced strain on that region will play a dominant role controlling the failure response of armor welds produced with HLAW.

#### Acknowledgments

The authors wish to thank Adres Acuna and Prof. Antonio Ramirez (The Ohio State University) for performing the hardness measurements; Ross Rentz and Ken Talley (NIST) for assistance in performing mechanical testing; and Terrence Udovic and Thomas Gnaeupel-Herold (NCNR) for assistance with annealing and helpful discussions.

## 5. References

- [1] Mahrle A, Beyer E (2006) Hybrid laser beam welding—Classification, characteristics and applications. *Journal of Laser Applications* 18:169–180. <https://doi.org/10.2351/1.2227012>
- [2] Madhusudhan Reddy G, Mohandas T (1996) Ballistics performance of high-strength low-alloy steel weldments. *Journal of Materials Processing Technology* 57:23–30. [https://doi.org/10.1016/0924-0136\(95\)02041-1](https://doi.org/10.1016/0924-0136(95)02041-1)
- [3] Madhusudhan Reddy G, Mohandas T, Papukutty KK (1998) Effect of welding process on the ballistic performance of high-strength low-alloy steel weldments. *Journal of Materials Processing Technology* 74:27–35. [https://doi.org/10.1016/S0924-0136\(97\)00245-8](https://doi.org/10.1016/S0924-0136(97)00245-8)
- [4] Bassett J (1998) Laser welding of high hardness armour steel. *Science and Technology of Welding and Joining* 3:244–248.
- [5] Roepke C, Liu S (2009) *Weld Journal* 88:159–167. <https://doi.org/10.1179/stw.1998.3.5.244>
- [6] Grujicic M, Ramaswami S, Snipes JS, Yen CF, Cheeseman BA, Montgomery JS (2013) Multiphysics modeling and simulations of Mil A46100 armor-grade martensitic steel gas metal arc welding process. *Journal of Materials Engineering and Performance* 22:2950–2969. <https://doi.org/10.1007/s11665-013-0583-2>
- [7] Mazar Atabaki M, Ma J, Yang G, Kovacevic R (2014) Hybrid laser/arc welding of advanced high strength steel in different butt joint configurations. *Materials & Design* 64:573–587. <https://doi.org/10.1016/j.matdes.2014.08.011>
- [8] Grujicic M, Snipes JS, Galgalikar R, Ramaswami S, Yavari R, Yen CF, Cheeseman BA (2014) Ballistic-failure mechanisms in gas metal arc welds of Mil A46100 armor-grade steel: A computational investigation. *Journal of Materials Engineering and Performance* 23:3108–3125. <https://doi.org/10.1007/s11665-014-1090-9>
- [9] Kong F, Ma J, Kovacevic R (2011) Numerical and experimental study of thermally induced residual stress in the hybrid laser–GMA welding process. *Journal of Materials Processing Technology* 211:1102–1111. <https://doi.org/10.1016/j.jmatprotec.2011.01.012>
- [10] Wells MGH, Weiss RK, Montgomery JS, Melvin TG (1992) in *U.S. Army Tank-Automotive Command*.
- [11] Ribic B, Palmer TA, DebRoy T (2009) Problems and issues in laser-arc hybrid welding. *International Materials Reviews* 54:223–244. <https://doi.org/10.1179/174328009X411163>
- [12] Moore PL, Howse DS, Wallach ER (2004) Microstructures and properties of laser/arc hybrid welds and autogenous laser welds in pipeline steels. *Science and Technology of Welding and Joining* 9:314–322. <https://doi.org/10.1179/136217104225021652>
- [13] Santisteban JR, Edwards L, Fitzpatrick ME, Steuwer A, Withers PJ, Daymond MR, Johnson MW, Rhodes N, Schooneveld EM (2002) Strain imaging by Bragg edge neutron transmission. *Nuclear Instruments and Methods in Physics Research A* 481:765–768. [https://doi.org/10.1016/S0168-9002\(01\)01256-6](https://doi.org/10.1016/S0168-9002(01)01256-6)
- [14] Kockelmann W, Frei G, Lehmann EH, Vontobel P, Santisteban JR (2007) Energy-selective neutron transmission imaging at a pulsed source. *Nuclear Instruments and Methods in Physics Research A* 578:421–434. <https://doi.org/10.1016/j.nima.2007.05.207>
- [15] Vogel S, Bourke M, Hanan J, Priesmeyer H, Üstündag E (2001) Non-destructive in-situ real-time measurements of structural phase transitions using neutron transmission. *Advances in X-ray Analysis* 44:75–84.
- [16] Kim SA, Johnson WL (2007) Elastic constants and internal friction of martensitic steel, ferritic-pearlitic steel, and  $\alpha$ -iron. *Materials Science and Engineering A* 452–453:633–639. <https://doi.org/10.1016/j.msea.2006.11.147>

**About the authors:** Jeffrey W. Sowards conducted this work as a member of the Applied Chemicals and Materials Division at NIST in Boulder and is now a welding engineer at NASA, Marshall Space Flight Center. Daniel S. Hussey and David L. Jacobson are physicists in the Radiation Physics Division at NIST. Stan Ream is a welding engineer at EWI. Paul Williams is a physicist in the Applied Physics Division at NIST. The National Institute of Standards and Technology is an agency of the U.S. Department of Commerce.